Stacked Nanoporous Anodic Alumina Gradient-Index Filters with Tunable Multi-Spectral Photonic Stopbands as Sensing Platforms

Laura K Acosta[†], *Francesc Bertó-Roselló*[†] , *Elisabet Xifre-Perez*[†], *Abel Santos* [✗‡§] *Josep Ferré-Borrull*[†] *and Lluis F. Marsal*[†*]

[†] Departament d'Enginyeria Electrònica, Elèctrica i Automàtica, Universitat Rovira i Virgili,

Avinguda Països Catalans 26, 43007 Tarragona, Spain

[✗] School of Chemical Engineering, The University of Adelaide, Adelaide, South Australia 5005, Australia

[‡] Institute for Photonics and Advanced Sensing (IPAS), The University of Adelaide, Adelaide, South Australia 5005, Australia

[§] ARC Centre of Excellence for Nanoscale BioPhotonics (CNBP), The University of Adelaide, Adelaide, South Australia 5005, Australia

KEYWORDS: nanoporous anodic alumina, photonic crystals, stacked, gradient index filters, multispectral bands, sensing platforms

Abstract

This study presents the development and optical engineering of stacked nanoporous anodic alumina gradient-index (NAA-GIFs) filters with tunable multi-spectral photonic stopbands for sensing applications. The structure of these photonic crystal (PC) is formed by stacked layers

of NAA produced with sinusoidally modified effective medium. The progressive modification of the sinusoidal period during the anodization process enables the generation and precise tuning of the characteristic photonic stopbands (PSB) (i.e. one per sinusoidal period in the anodization profile) of these PC structures. Four types of NAA-GIFs featuring three distinctive PSBs positioned within the visible spectral region are developed. The sensitivity of the effective medium of these NAA-GIFs is systematically assessed by measuring spectral shifts in the characteristic PSBs upon infiltration of their nanoporous structure with analytical solutions of D-glucose with several concentrations (0.025 – 1 M). This study provides new insights into the intrinsic relationship between the nanoporous architecture of these PCs and their optical properties, generating opportunities to fabricate advanced optical sensing systems for high-throughput and multiplexed detection of analytes in a single sensing platform.

1. INTRODUCTION

The design and engineering of nanostructures with innovative architectures and materials can pave the way for controlling light-matter interactions at the nanoscale in novel ways. These nanostructures would enable new opportunities to develop advanced materials for a plethora of applications, including optical chemical and biosensing[1–4], drug delivery[5,6], and photonic encryption[7]. Photonic crystals (PCs)

are a class of optical nanostructures with allowed and forbidden photonic bands that modify the movement of photons by altering the dispersion of electromagnetic waves when photons travel across de PC´s structure. PCs modulate the flow of light when photons travel across the material. These light-matter interactions can be tuned with accuracy by engineering the PC´s structure, which features regularly distributed regions of high and low refractive index in one, two or three dimensions [8–16]. PCs can be produced with different architectures and materials to attain light modulation across the broad range of spectral regions (from UV to IR), depending on the application needs [17–22].

Of all PC architectures, gradient index filters (GIFs) are PCs that are typically used as selective filters due to their narrow photonic band.[23] These photonic structures have also been explored as platforms to develop highly sensitive optical sensors.[24] When the effective medium of gradient-index filters is changed, the characteristic band undergoes spectral shifts that can be used as sensing principle for a variety of optical sensing systems.[25]

Nanoporous anodic alumina (NAA) is a promising base material for the fabrication of PCs. NAA is formed by the electrochemical oxidation (anodization) of aluminum, a cost-effective and fully scalable process compatible with conventional micro- and nanofabrication approaches that allows the precise control over the geometry and distribution of the pores[26,27]. The optical properties of NAA rely intrinsically upon its nanoporous architecture. Therefore, to engineer the nanoporous structure of NAA provides novel means of modulating its refractive index in a multi-dimensional fashion to fabricate advanced materials with unique optical properties to guide, reflect, transmit, emit, and enhance incidence light.[28,29]. Furthermore, NAA has high chemical and physical stability, provides stable optical signals without further surface passivation and its surface chemistry can be easily modified with a broad range of functional molecules for multiple applications, including chemo- and biosensing, drug delivery, optical encoding, theranostics implants[30,31], catalysis and electromagnetism[32,33].

NAA is particularly interesting for the development of optical sensing platforms since it is optically active (i.e. can alter the motion of photons in different ways) and its nanopores can work as nanocontainers to accommodate analytes of interest. NAA can be modified with functional molecules to provide selectivity toward a broad range of analytes and its nanopore geometry can be engineered to increase the effective surface area for binding events. [34–43]

To fabricate PCs with multiple narrow photonic stopbands at different spectral positions remains challenging and to date, only a few proof-of-concept studies have realized this class of PCs. For instance, Sailor et al [44,45] and Santos et al [46] developed porous silicon and NAA-PC structures respectively with multiple photonic stopbands at different spectral positions. These PCs were obtained by averaging the sum of multiple sinusoidal waves into a single complex waveform, which was subsequently translated into anodization profiles to engineer the nanoporous structure of these PCs in depth. Each sinusoidal wave determines the position and the reflectance amplitude of a forbidden photonic band or photonic stopband. Multiple-band NAA structures have interesting applications such as optical encoding tags, optical sensing, photonics and photovoltaics [44,47–53]. However, the average sum of multiple sinusoidal waves and their implementation into anodization processes that are effectively translated into modulations of effective refractive index present some limiting drawbacks. When the number of forbidden bands is increased, the reflectance amplitude of each band is reduced. The reflectance amplitude of each forbidden band is proportional to the amplitude of the sinusoidal wave. Therefore, when the number of bands increases, the multiple averaging reduces the amplitude of each sinusoidal wave proportionally to the number of bands, thus decreasing the reflectance amplitude of all the bands in the spectrum of these PCs. Therefore, this fabrication approach is amplitude-limited and do not offer enough controllability to generate multiple spectral forbidden bands with high intensity. To overcome this limitation, in this work we devise an alternative fabrication method that enables the production of NAA-based PCs featuring multiple forbidden bands at specific spectral positions with higher intensity. Multiple sinusoidal current density waveforms of different period are applied sequentially during anodization to produce composite NAA-PC structures composed of stacked NAA-GIFs. In contrast to previous methods using complex

averaged waveforms, the sequential application of sinusoidal anodizing current density periods provides a suitable means of creating NAA-PCs with multiple forbidden bands with high intensity. The flexibility of this novel fabrication method to design and engineer the tunability of multi-spectral photonic stopband in these NAA-PCs is evaluated in real-time. The sensitivity of the effective medium of these PC structures upon changes of the medium filling the pores is systematically assessed to demonstrate the potential of these NAA-PCs as optical sensing platforms.

2. EXPERIMENTAL

2.1 Materials

High purity aluminum discs (Al) (thickness 0.5 mm and purity 99.99%) were acquired from Goodfellow Cambridge Ltd (UK), acetone ($(CH_3)_2CO$), ethanol (C_2H_5OH), perchloric acid ($HClO_4$), oxalic acid ($H_2C_2O_4$), hydrochloric acid (HCl), copper chloride ($CuCl_2$) and D-glucose ($C_6H_{12}O_6$) were provided by Sigma-Aldrich. Double deionized water (DI) (18.6 MΩ) was used for all the solutions unless otherwise specified.

2.2 Fabrication of Multi-Spectral NAA-GIFs

Aluminum substrates were cleaned with acetone, water, and ethanol in order to remove all the impurities and grease. Before anodization, aluminum substrates were electropolished in a solution 4:1 v/v of ethanol-perchloric acid at 20 V and 5°C for 6 min, with the stirring

direction alternated every 60 s. Subsequently, anodization of aluminum substrates was carried out in oxalic acid 0.3 M at 5°C by applying a current density–time anodization waveform that modulates the pore diameter in depth, as the NAA layer grows. Finally, the remaining aluminum was removed from the backside of the NAA-GIFs by chemical etching with a saturated solution of HCl and $CuCl_2$ for optical characterization.

A set of anodization profiles were generated to produce NAA-GIFs with three forbidden bands positioned at specific wavelengths within the visible region of the spectrum following Equation 1. For this purpose, the anodization current density waveform was formed by three sequential sinusoids with three different pulse periods (i.e. T_1, T_2 and T_3). The rest of the sinusoid parameters such as offset current density (J_0), current density amplitude (J_1) and number de periods (N) were kept constant for all the sinusoids. Table 1 summarizes the fabrication conditions of the different NAA-GIFs produced in this study. The anodization current density waveform profile follows equation 1:

$$J(t) = \begin{cases} J_1 \sin\left(\frac{2\pi}{T_1}\right) + J_0 & 0 \le t < NT_1 \\ J_1 \sin\left(\frac{2\pi}{T_2}\right) + J_0 & NT_1 \le t < NT_2 \\ J_1 \sin\left(\frac{2\pi}{T_3}\right) + J_0 & NT_2 \le t < NT_3 \end{cases} \quad (1)$$

where J(t) is the anodization current density at time t, J_1 is the current density amplitude, T_i (i = 1, 2, 3) is the anodization period and J_0 is the offset current density. Figure 1a shows a conceptual illustration of the fabrication process used to generate multi-spectral NAA-GIFs including a representative anodization profile (Figure 1b) and schematics of the different layers composing the structure of NAA-GIFs with the corresponding anodization period and the reflection spectrum of a NAA-GIFs with J_0 = 2.6 $mAcm^{-2}$, J_1= 1.3 $mAcm^{-2}$, T_1 = 150, T_2 = 175 and T_3 = 200 s, and N = 100 periods and J_0 = 2.6 $mAcm^{-2}$, J_1= 1.3 $mAcm^{-2}$, T_1 = 170, T_2 = 175 and T_3 = 180 s, and N = 100 periods, with details of the characteristics reflection stop bands (Figure 1c)

Table 1. Summary of fabrication conditions and period thicknesses of NAA-GIFs.

Sample	J_0 [mAcm^2]	J_1 [mAcm^2]	T_1 [s]	T_2 [s]	T_3 [s]	N	Period Thickness [nm]		
							Layer 1 (T1)	Layer 2 (T2)	Layer 3 (T3)
NAA-GIFs-A	2.6	1.3	150	175	200	100	180	210	240
NAA-GIFs-B	2.6	1.3	160	175	190	100	192	210	228
NAA-GIFs-C	2.6	1.3	165	175	185	100	198	210	222
NAA-GIFs-D	2.6	1.3	170	175	180	100	204	210	216

a) Fabrication of NAA-GIFs

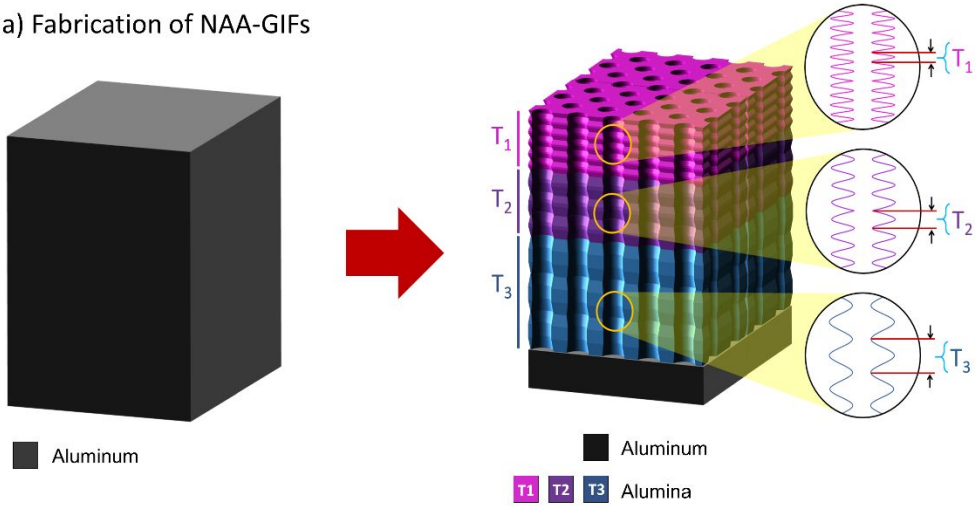

b) Sinusoidal anodization profile of NAA-GIFs

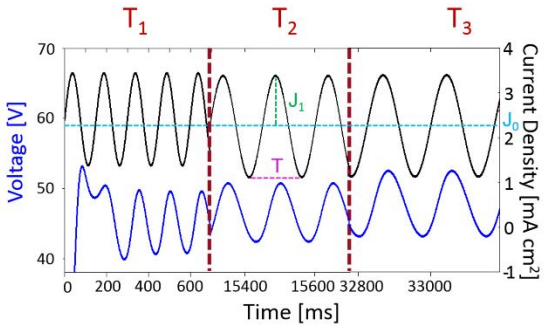

c) Relationship between nanoporous architecture and optical properties of NAA-GIFs

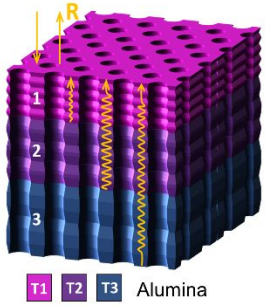

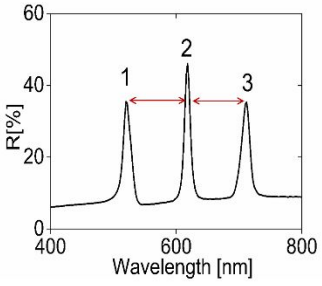

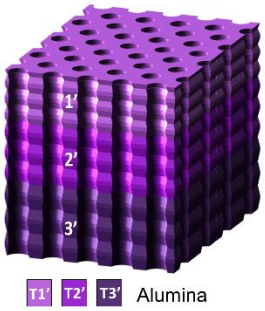

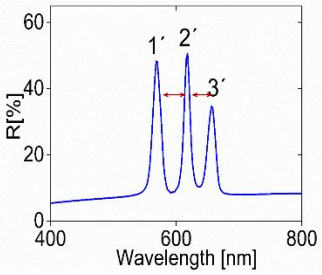

Figure 1.Conceptual illustration of the electrochemical approach used to produce multi-spectral NAA-GIFs by sinusoidal current density profile for three photonic stopbands. (a) Fabrication process of multi-spectral NAA-GIFs. (b) Sinusoidal anodization profile of a representative multi-spectral NAA-GIF. (c) Schematics showing the existing relationship between nanoporous architecture and optical properties of multi-spectral NAA-GIFs for the samples produced with J_0 = 2.6 $mAcm^{-2}$, J_1= 1.3 $mAcm^{-2}$, T_1 =150, T_2 =175 and T_3 =200 s, and N = 100 periods, and J_0 = 2.6 $mAcm^{-2}$, J_1= 1.3 $mAcm^{-2}$, T_1 =170, T_2 =175 and T_3 =180 s, and N = 100 periods.

A pore widening treatment was performed after anodization in order to widen the nanopore diameter in each NAA-GIFs and study the influence of the porosity on their optical properties by wet chemical etching in H_3PO_4 5% wt at 35ºC. The pore widening treatment was applied for different times, from 0 to 25 min, in an interval of 5 min.

2.3 Optical Characterization of Multi-Spectral NAA-GIFs

The reflection spectra of multi-spectral NAA-GIFs across the UV-visible-NIR spectrum were measured at 8º of incidence angle with a resolution of 2 nm in a Perkin Elmer UV-Visible-NIR Lambda 950 spectrophotometer.

The effective medium of these NAA-PCs was assessed in real-time by quantifying spectral shifts in the positions of the characteristics photonic stopbands of NAA-GIFs upon infiltration with D-glucose solutions of different refractive index. This process was performed in real-time in a flow cell made of acrylic plastic. Reflectance spectra of multi-spectral NAA-GIFs were obtained using a halogen light source and a spectrometer. Light was directed onto the surface of NAA-GIFs at normal angle through a bifurcated fiber optic cable consisting of six illuminating waveguides and one reading waveguide coupled to an optical lens that focused the light on the top of the NAA-GIFs. The

light reflected was collected by the spectrometer, which recorded one spectrum every 2 s. Reflectance spectra were acquired for the wavelength range 400-800 nm.

The sensitivity of the effective medium of the NAA-GIFs was assessed by infiltrating their nanoporous structure with glucose solutions at different concentrations (0.025, 0.05, 0.125, 0.250, 0.50, 0.75, and 1M). Upon the infiltration, the characteristic forbidden bands undergo spectral shifts due to changes in the refractive index of the medium filling the nanopores. These changes are quantified in real time using deionized water (DI) as a baseline at constant rate of 500 μl min^{-1}, between each infiltration a washing step with (DI).

The interferometric color of multi-spectral NAA-GIFs was characterized by digital pictures, acquired by a Canon EOS 700D digital camera equipped with Tamron 90 mm F2.8 VC USD macro mount lens with autofocus function under natural light illumination.

2.4 Structural Characterization of Multi-Spectral NAA-GIFs

The structural characterization of multi-spectral NAA-GIFs was performed using an environmental scanning electron microscope (ESEM FEI Quanta 600) operating at an accelerating voltage between 20 and 25 keV. ESEM images were analyzed by ImageJ software.

2.5 Modelling of Multi-Spectral NAA-GIFs

The optical properties of multi-spectral NAA-GIFs were modelled using an effective medium approximation (EMA) and the transfer matrix method (TMM). The effective refractive index of each layer in the structure of NAA-GIFs was calculated using the Looyenga-Landau-Lifshitz (3L) formula in combination with that reported from Bartzsch et al.[54,55] Calculation of the reflectance spectra was performed by means of the transfer matrix method using MatLab® software.

3. RESULTS AND DISCUSSION

3.1 Fabrication and structural Characterization of NAA-GIFs

Figure 2 shows a representative anodization current density profile for each T_i applied during the fabrication of multi-spectral NAA-GIFs and the measured voltage response of the system. This graph reveals that the anodization voltage (output) follows the sinusoidal variations of the applied anodization current density (input) with a certain delay. Anodization is an electrochemical process that relies on the flow of the electronic and ionic species across the oxide barrier layer located at the nanopores' bottom. Dynamic modifications of the anodizing current density alter the steady flow of electronic and ionic species across the oxide barrier layer, which needs a recovery time to achieve its equilibrium state again. This time delay depends on the thickness of the oxide barrier layer and the level of anodizing current density change[20,56,57]. It is remarkable that the amplitude of the measured voltage increases with the anodization period (i.e. T_1, T_2 and T_3) despite of keeping constant the rest of the parameters (J_0 and J_1). From this analysis, it is inferred that the porous layer growth has a dynamic behavior governed by a characteristic reaction time established by the anodization period.

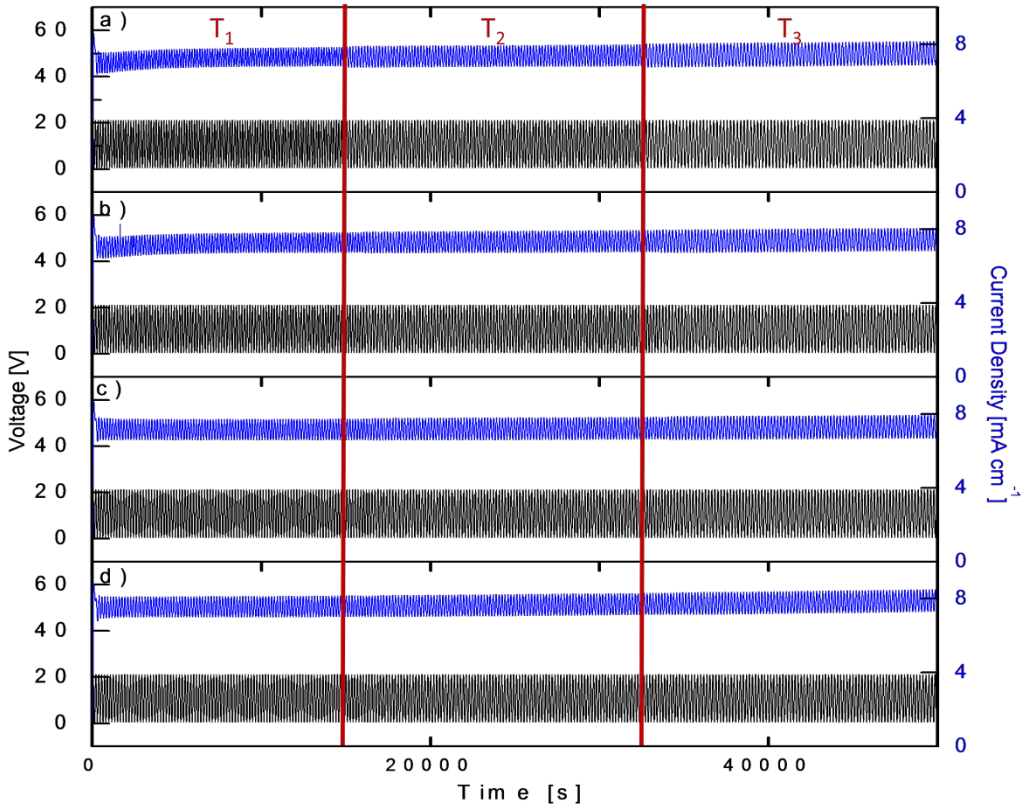

Figure 2. Evolution of the anodization current density and voltage during the fabrication of NAA-GIFs. (a) Anodization voltage and current density profile of sample NAA-GIFs-A J_0 = 2.6 $mAcm^{-2}$, J_1= 1.3 $mAcm^{-2}$, T_1 = 150, T_2 = 175 and T_3 = 200 s and N = 100 periods. (b) NAA-GIFs-B J_0 = 2.6 $mAcm^{-2}$, J_1= 1.3 $mAcm^{-2}$, T_1= 160, T_2= 175 and T_3 =190 s and N= 100 periods. (c) NAA-GIFs-C J_0 = 2.6 $mAcm^{-2}$, J_1= 1.3 $mAcm^{-2}$, T_1= 165, T_2= 175 and T_3 =185 s and N= 100 periods. (d) NAA-GIFs-D J_0 = 2.6 $mAcm^{-2}$, J_1= 1.3 $mAcm^{-2}$, T_1= 170, T_2 = 175 and T_3 = 180 s and N= 100 periods.

The anodization current density sinusoidal waves featuring three sequentially increasing anodization periods are translated into the material's structure as stacked PCs based on NAA-GIFs in the same structure. For each NAA-PC embedded within the structure of the multi-spectral NAA-GIF, the pore diameter varies sinusoidally in depth. The optical response of the composite NAA-GIFs presents several forbidden bands, one for each NAA-GIF composing the overall PC structure. Figure 3 shows representative ESEM images of a representative multi-spectral NAA-GIF produced in this study. The top view image shows nanopores randomly distributed across the surface of the PC structure (Figure 4a) the pore average of this sample (NAA-GIFs-A) is ~45 nm due to the pore widening treatment of 10 minutes. The pore diameter can be precisely controlled by the pore widening time from 0, 5, 10, 15, 20 and 25 min, which correspond to pore diameters of 35, 40, 45, 50, 55 and 60 nm, respectively (Figure S1 in Supporting Information). The general cross section of the samples shown in Figure 3b reveals the oscillating pattern in depth of the pore diameter. Figure 3c shows a magnified view of the yellow circle in figure 3b. The pore morphology of the NAA-GIFs induces a modification in depth of the porosity, which results in a sinusoidal variation of the effective refractive index in depth. An EMA (effective medium approximation) model was employed to design the NAA-GIFs structure as a multilayer system and provide a mechanistic explanation of the optical properties of multi-spectral NAA-GIFs. Figure 4 shows an illustration of the transition of the NAA-GIFs pore morphology into an effective graded-index model that follows the pore growth direction. This system is composed of multiple layers with constant refractive index which oscillate between a high refractive index and a low refractive index values along the nanopore's length.

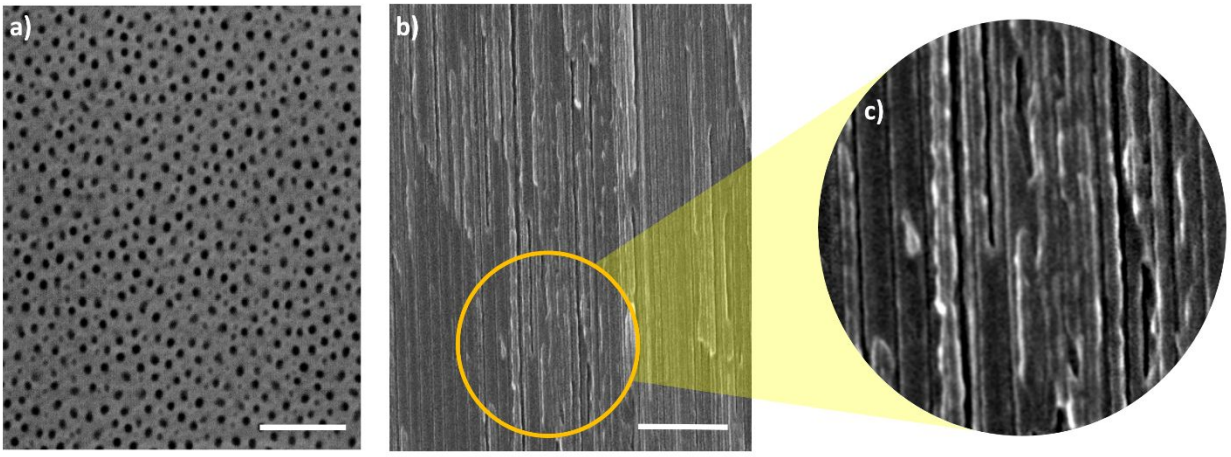

Figure 3. Structural characterization of a NAA-GIFs- produced with offset density current J_0= 2.6 mAcm^{-2}, amplitude density current J_1=1.3 mAcm^{-2}, N = 100 periods, T_1= 150, T_2=175, T_3= 200 s and pore widening time of 10 min (a) ESEM top view (scale bar: 1 μm). (b) ESEM General cross section (scale bar: 2 μm). (c) Magnified view of yellow circle.

Figure 4. Transition of the NAA-GIF nanopore morphology towards a multilayered system in which the constant effective refractive index of each layer varies between $n_{eff-low}$ and $n_{eff-high}$.

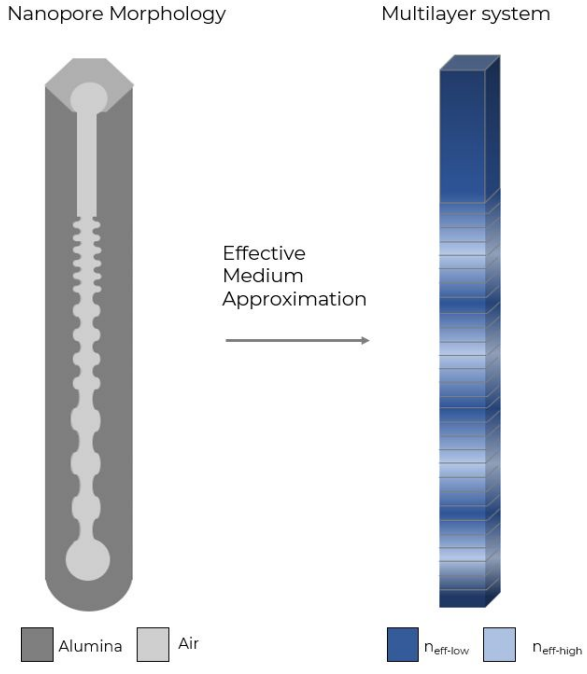

Multi-spectral NAA-GIFs fabricated in this study present three different forbidden bands, the spectral position of which is established by the anodization period T_i (i=1,2,3). The central anodization period T_2 is kept constant (T_2= 175 s), which means that the position of the central band is approximately the same for all the NAA-GIFs. However, the values of the other two periods (T_1 and T_3 were systematically modified in each multi-spectral NAA-GIF in order to demonstrate the tuneability of the bands separation and its effect on the sensitivity of these composite PCs. As summarized in Table 1, NAA-GIFs-A were produced with T_1= 150, T_2= 175 and T_3= 200 s, NAA-GIFs-B were fabricated with T_1= 160, T_2= 175 and T_3=190 s, NAA-GIFs-C with T_1= 165, T_2= 175 and T_3= 185 s and NAA-GIFs-D with T_1= 170, T_2= 175 and T_3=180 s.

3.2 Optical characterization and modelling of NAA-GIFs

All the studied multi-spectral NAA-GIFs were fabricated with J_0=2.6 mAcm^{-2}, J_1= 1.3 mAcm^{-2} with constant number of periods (N = 100 periods) whereas the values of the three periods T_i vary from one to the other. Figure 5a shows the reflectance spectra of multi-spectral NAA-GIFs with varying T_i. Three forbidden bands can be clearly observed for all these NAA-GIFs, which show a narrow width, with an average of full width and half maximum (FWHM) between 12 to 20 nm. It can be observed that the central forbidden band is positioned at the same wavelength for all the multi-spectral NAA-GIFs since all of them were fabricated with the same T_2 (175 s). On the contrary, T_1 and T_3 were systematically modified to demonstrate the tuneability of this class of PC system across the visible spectrum. The position of the forbidden bands depends on the anodization period, which can be precisely tuned by increasing or decreasing T_1 and T_3 (i.e. red shift –move towards longer wavelengths or blue shift move towards shorter wavelengths). Figure 5a shows the position of the forbidden bands for four different combinations of anodization periods. The excellent repeatability and controllability of the anodization system is observed in this graph as all the NAA-GIFs- present a central forbidden band at 618 ± 1 nm, which is associated with the NAA-GIF produced with T_2= 175 s. For the NAA-GIFs-A, the position of the reflection bands for T_1 = 150 s, T_2 = 175 s, T_3 = 200 s were located at in the 520, 618 and 712 nm, respectively. In the case of NAA-GIFs-B, the forbidden bands were located in 553, 616 and 673 nm, which correspond to

T_1=160 s, T_2 = 175 s and T_3 = 190 s, respectively. The position of the forbidden bands of NAA-GIFs-C produced with T_1= 165 s T_2= 175 s and T_3= 185 s were in 570, 618 and 660 nm, respectively. Finally, the reflection bands of NAA-GIFs-D were located in 596, 619 and 640 nm, which correspond to the embedded NAA-GIFs fabricated with T_1= 170 s, T_2= 175 s and T_3= 180 s. Figure 5b shows that the position of the three forbidden bands have a linear dependence with the corresponding anodization period (T_1, T_2 and T_3). These linear fitting make it possible to design the spectral fingerprint of each multi-spectral NAA-GIF (i.e. position of the forbidden bands) across the entire spectrum to fulfil the requirement of different applications. Digital images of these multi-spectral NAA-GIFs reveal that these PCs display vivid interferometric color, which is established by the position of the characteristic reflection bands. For the samples NAA-GIFs-A, C and D the interferometric color is red while the sample NAA-GIFs-B is green. The interferometric color exhibit by these photonics structures is established by the band located at longer wavelengths 712, 660 and 640 nm for samples NAA.GIFs-A, C, and D respectively and in the case of sample B the interferometric color is given by the closer wavelength 553 nm. Figure 5c shows a compilation of experimental and simulated reflection spectra for the multi-spectral NAA-GIFs fabricated in this study. The simulation results show that the three reflection bands of the multi-spectral NAA-GIF (cyan lines) are in good agreement with the experimental reflection spectra of the samples. These graphs show that the transfer matrix model developed in our study can precisely predict the spectral fingerprint of these complex PCs. This model provides a mechanistic explanation of the light–matter interactions occurring within these PCs, opening new opportunities to design novel PC architectures for specific applications.

a)

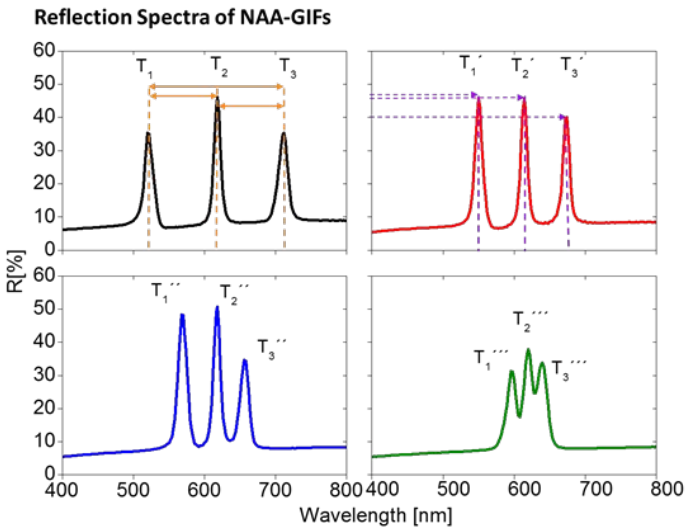
Reflection Spectra of NAA-GIFs
R[%]
Wavelength [nm]

b)

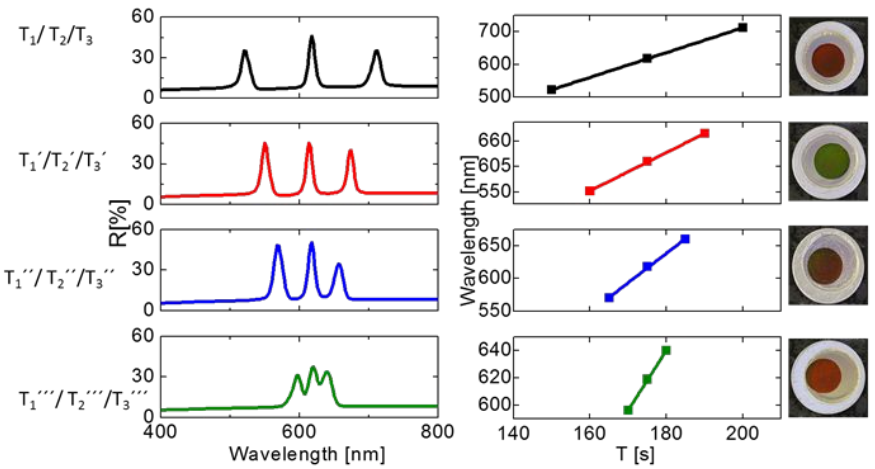
Linear fitting of dependence of position of the reflection bands on the period time
R[%]
Wavelength [nm]
T [s]

c)

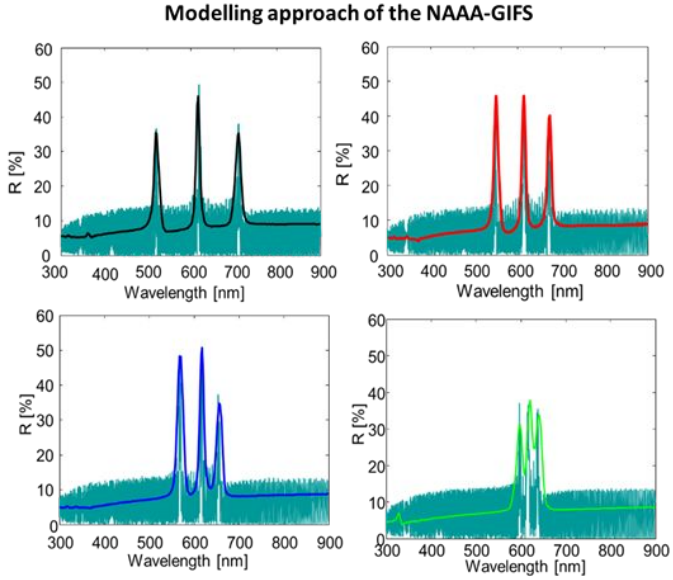
Modelling approach of the NAAA-GIFS
R [%]
Wavelength [nm]

Figure 5. Reflection spectra of NAA-GIFs of samples A-D (Described in table 1). (a) Reflection spectra of all samples (NAA-GIF-A-D). (b) Position of the reflection bands of NAA-GIFs in (a-d) as a function of period time (T). The linear regression is plotted for each NAA-GIFs. Digital pictures of NAA-GIFs A-D (c) Modelling approach of all the samples (NAA-GIFs-A-D) cyan lines represent the modelling approximation of the NAA-GIFs spectra and the black, red, blue and green represent de experimental spectra of samples.

3.3 Pore Widening Effect in the Optical Properties of Multi-Spectral NAA-GIFs.

To study the effect of the pore widening time on the optical properties of multi-spectral NAA-GIFs, the reflectance spectrum of these NAA-GIFs fabricated with J_0= 2.6 mAcm^{-2}, J_1= 1.3 mAcm^{-2} and T_1= 165, T_2 =170 and T_3=175 s was measured at different pore widening times (t_{pw}): 5, 10, 15, 20 and 25 min, which correspond to nanopore diameters of 35, 40, 45, 50, 55 and 60 nm, respectively (Figure 6). Table 2 and Figure 6 summarizes the effect of the six different tpw on the position of the forbidden bands, their intensity, and their FWHM. The position of the characteristic forbidden bands undergoes a blue shift when the PC structure is etched and the size of its nanopores is widened. Figure 6a shows the reflection spectra with t_{pw}. At t_{pw} = 0 (i.e. as-produced NAA-GIF, average of pore diameter ~35 nm) the position of the reflection bands was located at 578, 606 and 628 nm for T_1= 165 s, T_2= 170 s and T_3= 175 s, respectively. The reflection bands present a maximum reflection intensity of 32.3, 51.8 and 57.8 %, respectively, and a FWHM of 24, 18 and 16 nm. At t_{pw}= 5 min (i.e. pore diameter ~ 40nm), the reflection bands are blue-shifted to 568, 598 and 622 nm, the maximum reflection for these bands were 34.8, 55.2, 60.3 % and their FWHM were 31, 18 and 18 nm, respectively. In the case of t_{pw} = 10 min (i.e. average of pore diameter of 45 nm), the position of the forbidden bands was located at 558, 592 and 618 nm, the maximum reflection for these bands were 46.0, 54.8 and 46.5 %, and the FWHM were 32, 20 and 20 nm, respectively and. For t_{pw} = 15 min (average of pore diameter ~50 nm), the position of the forbidden bands was 546, 582 and 612 nm, the maximum reflection for these bands were 45.4, 52.8, and 43.8 %, and the FWHM of the bands were 35, 21 and 22 nm respectively. The position of the reflection bands for t_{pw} = 20 min (i.e. pore diameter ~55 nm) were 532, 572 and 602 nm, with a maximum reflection of 42.2, 49.7 and 44.3 % and FWHM of 42, 23 and 23 nm, respectively. At t_{pw}= 25 min (average

pore diameter of 60 nm), the position of the forbidden bands was situated at 520, 560 and 590 nm, the maximum reflection of the bands were 38.8, 46.1 and 41.3 % and the FWHM for these forbidden bands were 44, 24 and 24 nm, respectively. Figure 6b shows the linearity between t_{pw} and the position of the three forbidden bands. This graph indicates that the position of the forbidden bands blue shifts linearly when tpw increases from 0 to 25 min. However, the blue shift rate (i.e. slope of linear fitting) depends on the position of the forbidden band: the slope of band 1 is greater than that of bands 2 and 3. The slopes of the fitting lines for the three forbidden bands of multi-spectral NAA-GIFs produced were found to be -2.34 (T_1= 165 s), -1.46 (T_2 = 170 s) and -1.81 (T_3 = 175 s) nm min^{-1}. The relation between the t_{pw} and the FWHM is presented in Figure 6c. For band 1, we can observe that a high increment of the FWHM with t_{pw}, whereas for bands 2 and 3 the increment is less marked. For the three bands, the increment of FWHM depends linearly on the pore widening time. The slopes of the fitting lines for the FWHM of the three forbidden bands of multi-spectral NAA-GIFs produced with T_1 = 165 s, T_2 = 170 s and T_3 = 175 s, were found to be 0.78, 0.32 and 0.26 nm min^{-1}, respectively. The difference observed between band 1 and the rest of bands can be explained by observing the NAA structure of the multi-spectral NAA-GIFs. The three bands of these NAA-PCs are generated by three different NAA-GIFs stacked one over another. The NAA-GIF that generates band 1 is at the top of the composite multi-spectral NAA-GIFs structure. Chemical etching at the top part of the composite NAA-GIF is more effective than within the nanoporous structure due to limited diffusion of chemical species. Therefore, the top NAA-GIF structure is etched at a slightly faster rate than its counterparts located at lower positions within the composite NAA-GIF. This results in a differential etching rate that leads to distinct blue shifts in the position of the characteristic forbidden bands of the multi-spectral NAA-GIFs. Whereas the other two NAA-GIFs, generating bands 2 and 3, are underneath and their complete NAA structure is affected by the etching dissolution in a similar way.

The average pore diameter also affects the amplitude of the forbidden band and it's FWHM (Table 2). When increasing the average pore diameter from 35 to 60 nm, the FWHM of band 1 increases from 24 to 44 nm, for band 2 increases from 18 to 24 nm and for band 3 from 16 to 24 nm. The maximum reflectance of the bands increases with the pore diameter until 50 nm, after which the reflectance intensity

decreases. Therefore, two different response regions can be differentiated: the pore diameter increases the maximum reflectance of the forbidden band until 50 nm, and decreases beyond this pore size. This phenomenon can be associated with diffusive light scattering by the overall PC structure due to increased porosity.

Effect of the PW time on the position of the characteristic reflection bands of NAA-GIFs

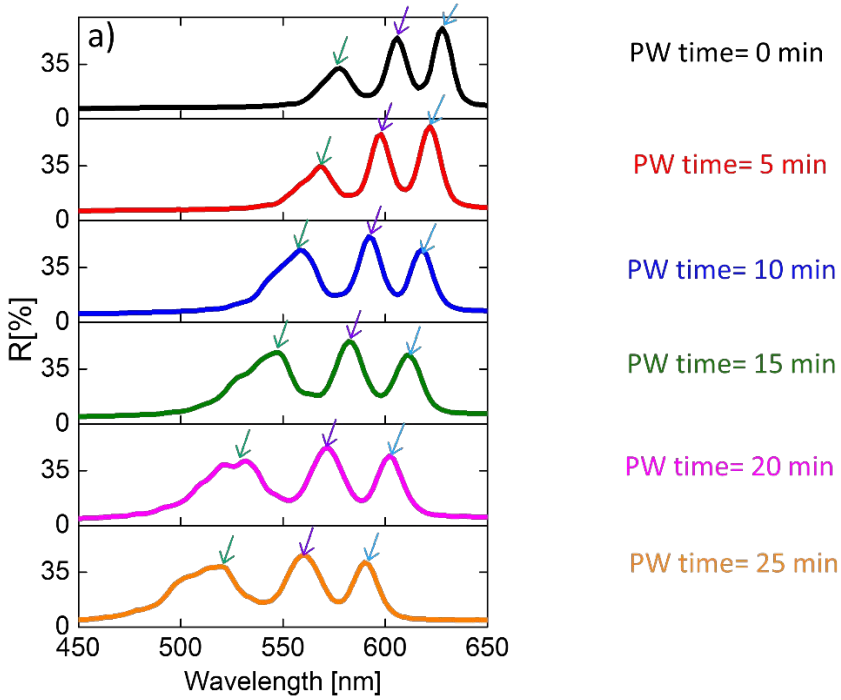

Linear fitting of wavelength dependence on PW time

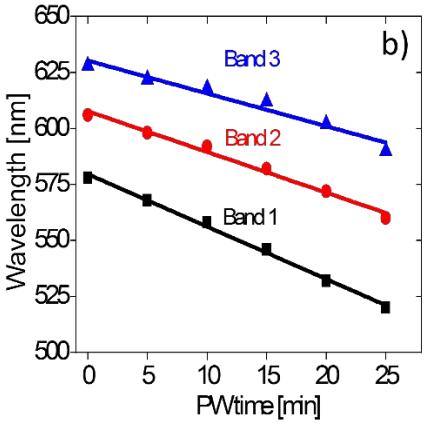

Linear fitting of FWHM dependence on PW time

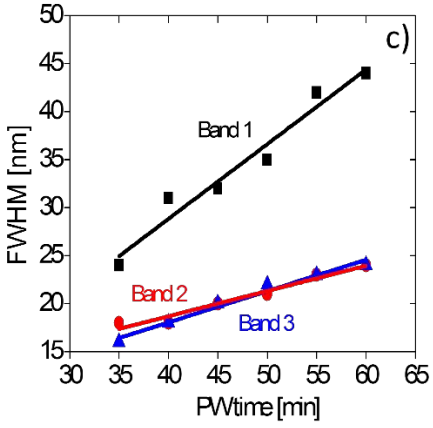

Figure 6. (a) Effect of the pore widening on the reflection spectrum of a NAA-GIFs with J_0= 2.6 mAcm^{-2}, J_1= 1.3 mAcm^{-2} and T_1= 165, T_2= 170 and T_3= 175 s was measured for different pore widening times: 0, 5, 10, 15, 20 and 25 min. (b) linear fitting lines showing the dependence between the position of the reflection bands and pore widening time (c) Linear fitting showing the dependence between Full width at half maximum (FWHM) and pore widening time.

Table 2. Summary of the effect of the pore widening on the reflectance spectrum of NAA-GIFs.

Pore widening time [min]	Average Pore diameter [nm]	Band	λ_{band} [nm]	R_{max} [%]	FWHM [nm]
0	35	1	578	32.3	24
		2	606	51.8	18
		3	628	57.8	16
5	40	1	568	34.8	31
		2	598	55.2	18
		3	622	60.3	18
10	45	1	558	46.0	32
		2	592	54.8	20
		3	618	46.5	20
15	50	1	546	45.4	35
		2	582	52.8	21
		3	612	43.8	22
20	55	1	532	41.2	42
		2	572	49.7	23
		3	602	44.3	23
25	60	1	520	38.8	44
		2	560	46.1	24
		3	590	41.3	24

3.4 Assessment of the Sensitivity of the Effective Medium of Multi-Spectral NAA-GIFs

To study the potential use of multi-spectral NAA-GIFs structures as sensing platforms, we assessed in real-time the spectral shifts in the three characteristic forbidden bands of these NAA-GIFs by filling the pores with analytical solutions D-glucose with different

concentrations. The variation of the effective refractive index of the medium filling the nanopores of multi-spectral NAA-GIFs red-shifts the position of the characteristic forbidden bands. These experiments were performed for different pore diameters in order to study the sensitivity of the PC structure when the pore diameter is increased. To this end, first a base line was obtained using deionized water, which was injected into the flow cell for 10 min until a stable base line was achieved. Then, analytical solutions of D-glucose 0.025 – 1.0 M were flowed at a constant rate of 500 μL min^{-1}. A cleaning step flowing fresh deionized water was carried out between each analytical solution of D-glucose in order to clean the remaining glucose molecules within the pores.

Figure 7 shows the assessment of sensitivity of the effective medium of multi-spectral NAA-GIFs. We can observe that the shift of the forbidden band positions increases when the D-glucose concentration increases, which indicates the utility of these PCs for sensing applications. Figure 7a shows a scheme of the infiltration of multi-spectral NAA-GIFs nanopores with different concentration of D-glucose. This infiltration produces a red shift (shift toward higher wavelengths) in the position of the forbidden bands. Figure7b shows the real-time measurements of a multi-spectral NAA-GIF with pore diameter of 40 nm (t_{pw} = 5 min). The results of the average of pore diameters of 35 (t_{pw}=0 min), 45(t_{pw}=10 min), 50 (t_{pw}=15 min) and 55 (t_{pw}=20 min) nm are shown in Figure S2 in the (Supporting Information). The infiltration of each analytical solution of D-glucose produces a redshift in the position of the bands. However, this change was reversible due to the lack of a chemical interaction between glucose molecules and the NAA-GIFs surface.

Figures 7c-e show the linear dependence between the shift of the forbidden bands and the concentration D-glucose for each pore diameter and band structure. Figure 7c shows the fitting lines for band 1 with reflection bands situated between 435 and 500 nm, which correspond to each pore widening time. The sensitivity (S) for each pore diameter in band 1 was 0.91 (35 nm), 1.64 (40 nm), 2.23 (45 nm), 3.15 (50 nm) and 3.07 (55 nm) nm M^{-1} and with a limit of detection of (LOD) 6.8, 1.3, 5.2, 3.5 and 5.5 mM, respectively. Figure 7d shows the results for band 2 (525-590 nm), the sensitivity (S) for each pore diameter of band 2 were 0.97 (35 nm), 1.64 (40 nm), 2.13 (45 nm), 2.90 (50 nm) and 3.23 (55 nm) nm M^{-1}, with a limit of detection of (LOD) 2.2, 1.9, 5.3, 3.7 and 2.8 mM, respectively. Figure 7e summarizes the

results for the band 3 (625-680 nm). The sensitivity (S) of each pore diameter of band 3 were 1.21 (35 nm), 1.63 (40 nm), 2.22 (45 nm), 2.87 (50 nm) and 3.38 (55 nm) nm M^{-1}, with a limit of detection of (LOD) 1.7, 1.8, 6.4, 3.7 and 1.7 mM, respectively. Table 3 summarizes the sensitivity and LOD characteristics of the multi-spectral NAA-GIFs obtained from the effective medium assessment. Figure 8 provides a bar chart comparing the sensitivity of the different PC structures. From these results, we can conclude that when the pore diameter in the structure of multi-spectral NAA-GIFs is increased, the shift of the forbidden band position increases linearly in all the cases, being more than three times greater for 55 nm than for 35 nm. Also, it is worthwhile noting that band 3 is in general more sensitive to effective refractive index variations than bands 1 and 2.

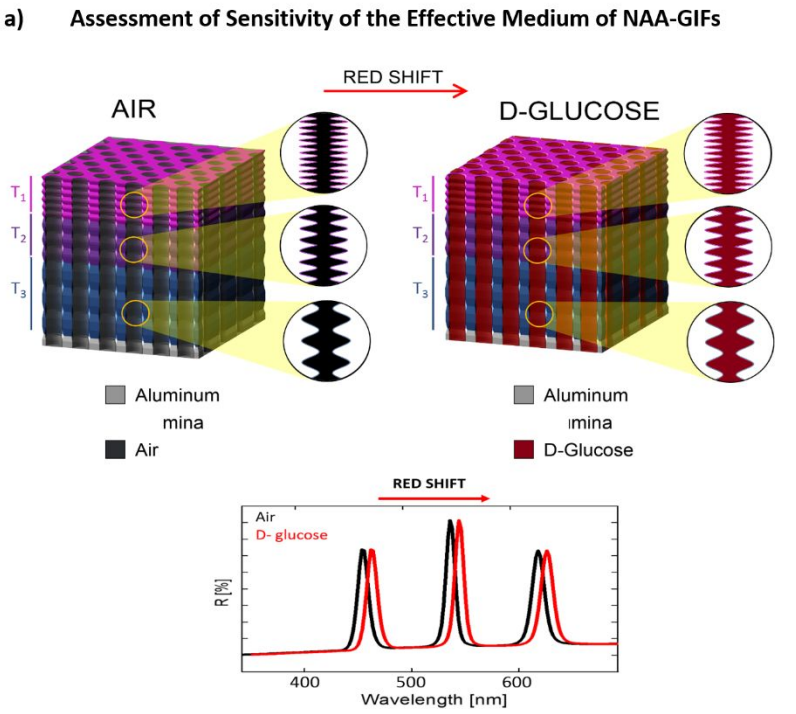
a) Assessment of Sensitivity of the Effective Medium of NAA-GIFs
RED SHIFT
AIR
D-GLUCOSE
T1
T2
T3
Aluminum
mina
Air
Aluminum
mina
D-Glucose
RED SHIFT
Air
D- glucose
R [%]
400
500
600
Wavelength [nm]

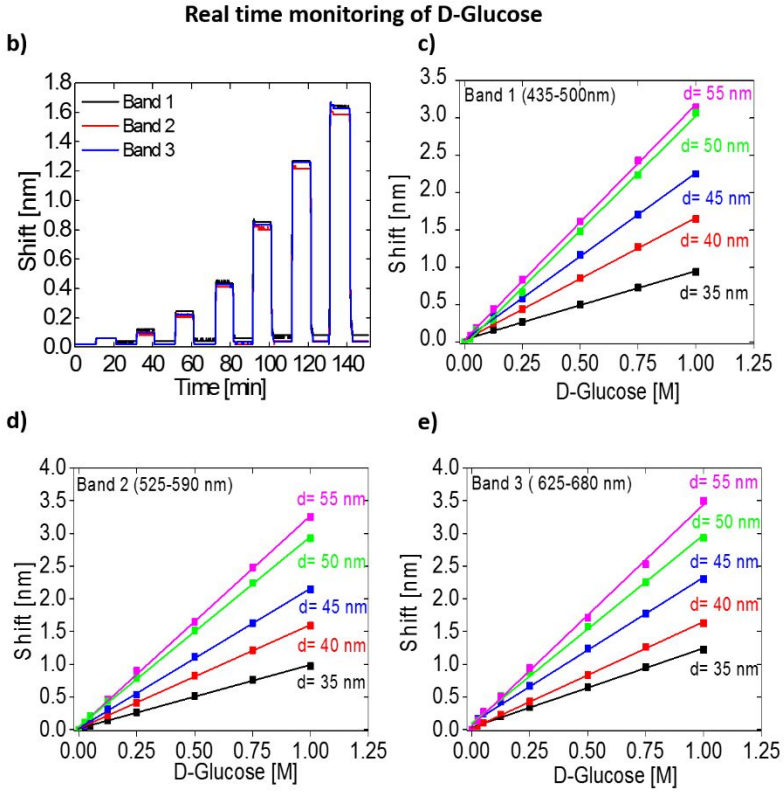
Real time monitoring of D-Glucose
b)
Band 1
Band 2
Band 3
Shift [nm]
Time [min]
c)
Band 1 (435-500nm)
d= 55 nm
d= 50 nm
d= 45 nm
d= 40 nm
d= 35 nm
Shift [nm]
D-Glucose [M]
d)
Band 2 (525-590 nm)
d= 55 nm
d= 50 nm
d= 45 nm
d= 40 nm
d= 35 nm
Shift [nm]
D-Glucose [M]
e)
Band 3 (625-680 nm)
d= 55 nm
d= 50 nm
d= 45 nm
d= 40 nm
d= 35 nm
Shift [nm]
D-Glucose [M]

Figure 7. (a) Assessment of the effective medium of NAA- GIFs. (b) Real time monitoring of D-Glucose concentrations 0.025, 0.05, 0.125, 0.25, 0.5, 0.75 and 1.0 M for 40 nm of pore diameter. Sensitivity approach for different pore diameters (35, 40, 45, 50 and 55 nm) for (c) band 1, (d) band 2, and (e) band 3

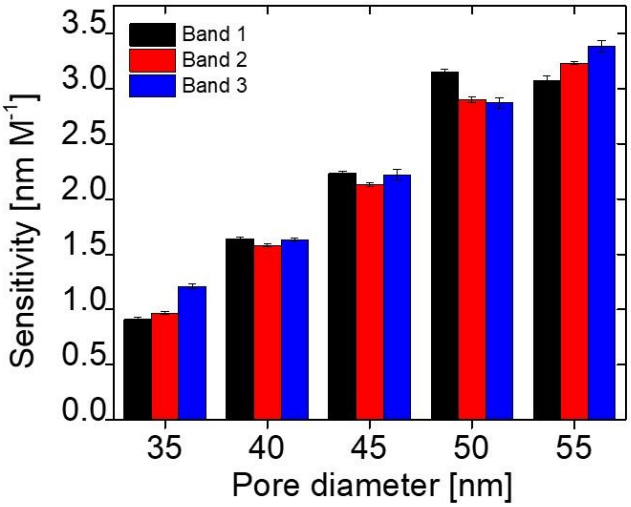

Figure 8. Sensitivity of each forbidden band of the NAA-GIFs for the different pore diameters (35, 40, 45, 50 and 55 nm) for the three bands.

Table 3. Sensitivity and limit of detection (LOD) of NAA-GIFs in the real time monitoring experiments.

Average Pore diameter [nm]	Band	S [nm M^{-1}]	LOD [mM]
D = 35 nm (t_{pw} = 0min)	1	0.91	6.8
	2	0.97	2.2
	3	1.21	1.7
D = 40 nm (t_{pw} = 5 min)	1	1.64	1.3
	2	1.58	1.9
	3	1.63	1.8
D = 45 nm (t_{pw}= 10 min)	1	2.23	5.2
	2	2.13	5.3
	3	2.22	6.4
D = 50 nm (t_{pw}= 15 min)	1	3.15	3.5
	2	2.90	3.7
	3	2.87	3.7
D = 55 nm (t_{pw}= 20 min)	1	3.07	5.5
	2	3.23	2.8
	3	3.38	1.7

4. CONCLUSIONS

In this work, we fabricated stacked photonic crystals based on nanoporous anodic alumina gradient-index filters (NAA-GIFs) with complex optical response by the application of successive sinusoidal anodization current density profiles. The position of the forbidden bands presented by these multi-spectral NAA-GIFs can be accurately tuned by varying the anodization period of the anodization current density waveform. Furthermore, we assess the effect of the porosity of the structure on the reflection spectrum by applying a pore widening chemical etching treatment from 0 to 25 min. The increment of the pore diameter blue-shifts the position of the forbidden bands. A lineal relation between the increments of the pore widening times and the position of the forbidden bands can be observed. The intensity and width of the bands also increases with the pore widening.

We also demonstrated the ability of multi-spectral NAA-GIFs structures for sensing applications by detecting small changes of the effective refractive index due to the fluid filling of the pores. Different concentrations of D-glucose have been successfully detected and quantified in real-time. These real-time experiments, carried out by increasing the average pore diameter from 35 nm to 55 nm, indicate that the sensitivity is different for each forbidden band and also it depends on the pore diameter of the multi-spectral NAA-GIF structure: the increment of the pore diameter leads to an enhancement in sensitivity of the photonic crystal structure.

ASSOCIATED CONTENT

Supporting information.

Additional information about the increment of pore diameter, including additional ESEM images and information of real-time spectral shifts for different pore diameters and concentrations of D-Glucose. (PDF)

AUTHOR INFORMATION

Corresponding Author

*Lluis F. Marsal

*E-mail: lluis.marsal@urv.cat. Phone: (+34) 977559625. Fax: (+34) 977 559605.

ORCID

Laura K. Acosta: 0000-0002-8729-3621

Francesc Bertó- Roselló: 0000-0002-0305-3314

Elisabet Xifré-Pérez: 0000-0001-6072-9889

Abel Santos: 0000-0002-5081-5684

Josep Ferré-Borrull: 0000-0002-5210-5133

Lluis F. Marsal: 0000-0002-5976-1408

Author Contributions

Ms. Laura K. Acosta carried out the experimental part of this work assisted by Dr. Elisabet Xifre-Perez and Dr. Josep Ferre-Borrull. Prof. Lluis F. Marsal conceived the idea and designed the experimental part of this work in collaboration with Dr. Abel Santos. Mr. Francesc Bertó-Roselló performed the theoretical calculations and simulations. The obtained results were discussed and analyzed by all the authors. The manuscript was written through contributions of all authors. All authors have given approval to the final version of the manuscript.

The manuscript was written through contributions of all authors.

Notes: The authors declare no competing financial interest.

ACKNOWLEDGMENTS

This work was supported by the Spanish Ministry of Economy and Competitiveness under grant number TEC2015-71324-R (MINECO/FEDER), the Catalan Government AGAUR 2017-SGR-1527 and the ICREA under the 2014-ICREA Academia Award.

Authors thank the support provided by the Australian Research Council (ARC) through the grant number CE140100003, the School of Chemical Engineering, the University of Adelaide (DVCR 'Research for Impact'initiative), the Institute for Photonics and Advanced Sensing (IPAS), and the ARC Centre of Excellence for Nanoscale BioPhotonics (CNBP).

ABBREVIATIONS

NAA nanoporous anodic alumina; PC Photonic Crystals, GIFs Gradient Index Filters, S Sensitivity; LOD Limit of detection; t_{pw} pore widening time; J_0 Offset current density; J_1 Amplitude current density; N Number of periods; T, Period time; PSB Photonic Stop Band; PW pore widening

REFERENCES

(1) Yan, P.; Fei, G. T.; Shang, G. L.; Wu, B.; De Zhang, L. Fabrication of One-Dimensional Alumina Photonic Crystals with a Narrow Band Gap and Their Application to High-Sensitivity Sensors. *Journal of Materials Chemistry C* **2013**, *1* (8), 1659–1664.

(2) Bonanno, L. M.; Segal, E. Nanostructured Porous Silicon-Polymer-Based Hybrids: From Biosensing to Drug Delivery. *Nanomedicine* **2011**, *6* (10), 1755–1770.

(3) Santos, A.; MacÍas, G.; Ferré-Borrull, J.; Pallarès, J.; Marsal, L. F. Photoluminescent Enzymatic Sensor Based on Nanoporous Anodic Alumina. *ACS Appl. Mater. Interfaces* **2012**, *4* (7), 3584–3588.

(4) Lee, J.; Bae, K.; Kang, G.; Choi, M.; Baek, S.; Yoo, D. S.; Lee, C. W.; Kim, K. Graded-Lattice AAO Photonic Crystal Heterostructure for High Q Refractive Index Sensing. *RSC Advances* **2015**, *5* (88), 71770–71777.

(5) Bonifacio, L. D.; Lotsch, B. V.; Puzzo, D. P.; Scotognella, F.; Ozin, G. A. Stacking the Nanochemistry Deck: Structural And Compositional Diversity in One-Dimensional Photonic Crystals. *Advanced Materials* **2009**, *21* (16), 1641–1646.

(6) Anglin, E. J.; Cheng, L.; Freeman, W. R.; Sailor, M. J. Porous Silicon in Drug Delivery Devices and Materials. *Advanced Drug Delivery Reviews* **2008**, *60* (11), 1266–1277.

(7) Santos, A.; Law, C. S.; Pereira, T.; Losic, D. Nanoporous Hard Data: Optical Encoding of Information within Nanoporous Anodic Alumina Photonic Crystals. *Nanoscale* **2016**, *8* (15), 8091–8100.

(8) Zaraska, L.; St□pniowski, W. J.; Ciepiela, E.; Sulka, G. D. The Effect of Anodizing Temperature on Structural Features and Hexagonal Arrangement of Nanopores in Alumina Synthesized by Two-Step Anodizing in Oxalic Acid. *Thin Solid Films* **2013**, *534*, 155–161.

(9) Yagur-Kroll, S.; Schreuder, E.; Ingham, C. J.; Heideman, R.; Rosen, R.; Belkin, S. A Miniature Porous Aluminum Oxide-Based Flow-Cell for Online Water Quality Monitoring Using Bacterial Sensor Cells. *Biosensors and Bioelectronics* **2014**, *64*, 625–632.

(10) Wang, G.; Wang, J.; Li, S. Y.; Zhang, J. W.; Wang, C. W. One-Dimensional Alumina Photonic Crystals with a Narrow Band Gap and Their Applications to High-Sensitivity Concentration Sensor and Photoluminescence Enhancement. *Superlattices and Microstructures* **2015**, *86*, 546–551.

(11) Wang, B.; Fei, G. T.; Wang, M.; Kong, M. G.; Zhang, L. De. Preparation of Photonic Crystals Made of Air Pores in Anodic Alumina. *Nanotechnology* **2007**, *18* (36), 1–4.

(12) Shu, S. W.; Zhang, J.; Tsang, C. K.; Shi, L. G.; Li, Y. Y. Metal-Based Rugate Filters with Strong Visible and near-Infrared Reflectivity. *Applied Physics B: Lasers and Optics* **2012**, *107* (3), 669–673.

(13) Pacholski, C. Photonic Crystal Sensors Based on Porous Silicon. *Sensors* **2013**, *13* (4), 4694–4713.

(14) Masuda, H.; Ohya, M.; Asoh, H.; Nakao, M.; Nohtomi, M.; Tamamura, T. Photonic Crystal Using Anodic Porous Alumina. *Japanese Journal of Applied Physics, Part 2: Letters* **1999**, *38*, 1403–1405.

(15) Macias, G.; Ferré-Borrull, J.; Pallarès, J.; Marsal, L. F. Effect of Pore Diameter in Nanoporous Anodic Alumina Optical Biosensors. *The Analyst* **2015**, *140*, 4848–4854.

(16) Gorelik, V. S.; Sverbil, P. P.; Filatov, V. V.; Bi, D.; Fei, G. T.; Xu, S. H. Transmission Spectra of One-Dimensional Porous Alumina Photonic Crystals. *Photonics and Nanostructures - Fundamentals and Applications* **2018**, *32*, 6–10.

(17) Toccafondi, C.; Thorat, S.; La Rocca, R.; Scarpellini, A.; Salerno, M.; Dante, S.; Das, G. Multifunctional Substrates of Thin Porous Alumina for Cell Biosensors. *Journal of Materials Science: Materials in Medicine* **2014**, *25* (10), 2411–2420.

(18) Santos, A.; Alba, M.; Rahman, M. M.; Formentin, P.; Ferre-Borrull, J.; Pallares, J.; Marsal, L. F. Structural Tuning of Photoluminescence in Nanoporous Anodic Alumina by Hard Anodization in Oxalic and Malonic Acids. *Nanoscale Research Letters* **2012**, *7* (1), 1–12.

(19) Law, C. S.; Lim, S. Y.; Santos, A. On the Precise Tuning of Optical Filtering Features in Nanoporous Anodic Alumina Distributed Bragg Reflectors. *Scientific Reports* **2018**, *8* (4642), 1–16.

(20) Montero-Moreno, J. M.; Belenguer, M.; Sarret, M.; Müller, C. M. Production of Alumina Templates Suitable for Electrodeposition of Nanostructures Using Stepped Techniques. *Electrochimica Acta* **2009**, *54* (9), 2529–2535.

(21) Sweetman, M. J.; Voelcker, N. H. Chemically Patterned Porous Silicon Photonic Crystals towards Internally Referenced Organic Vapour Sensors. *RSC Advances* **2012**, *2* (11), 4620–4622.

(22) Rahman, M. M.; Marsal, L. F.; Pallares, J.; Ferre-Borrull, J. Tuning the Photonic Stop Bands of Nanoporous Anodic Alumina-Based Distributed Bragg Reflectors by Pore Widening. *ACS Applied Materials and Interfaces* **2013**, *5* (24), 13375–13381.

(23) Lorenzo, E.; Oton, C. J.; Capuj, N. E.; Ghulinyan, M.; Navarro-Urrios, D.; Gaburro, Z.; Pavesi, L. Porous Silicon-Based Rugate Filters. *Applied optics* **2005**, *44* (26), 5415–5421.

(24) Nemati, M.; Santos, A.; Law, C. S.; Losic, D. Assessment of Binding Affinity between Drugs and Human Serum Albumin Using Nanoporous Anodic Alumina Photonic Crystals. *Analytical Chemistry* **2016**, *88* (11), 5971–5980.

(25) Siraji, A. A.; Zhao, Y. High-Sensitivity and High-Q-Factor Glass Photonic Crystal Cavity and Its Applications as Sensors. *Optics Letters* **2015**, *40* (7), 1508–1511.

(26) Masuda, Hideki and Fukuda, K. Ordered Metal Nanohole Arrays Made by Two-Step Replication of Honeycomb Structures of Anodic Alumina. *Science* **1995**, *268* (3), 1466–1468.

(27) Ferré-Borrull, J.; Pallarès, J.; Macías, G.; Marsal, L. F. Nanostructural Engineering of Nanoporous Anodic Alumina for Biosensing Applications. *Materials* **2014**, *7* (7), 5225–5253.

(28) Kumeria, T.; Santos, A.; Rahman, M. M.; Ferré-Borrull, J.; Marsal, L. F.; Losic, D. Advanced Structural Engineering of Nanoporous Photonic Structures: Tailoring Nanopore Architecture to Enhance Sensing Properties. *ACS Photonics* **2014**, *1* (12), 1298–1306.

(29) Md Jani, A. M.; Losic, D.; Voelcker, N. H. Nanoporous Anodic Aluminium Oxide: Advances in Surface Engineering and Emerging Applications. *Progress in Materials Science* **2013**, *58* (5), 636–704.

(30) Briggs, E. P.; Walpole, A. R.; Wilshaw, P. R.; Karlsson, M.; Pålsgård, E. Formation of Highly Adherent Nano-Porous Alumina on Ti-Based Substrates: A Novel Bone Implant Coating. *Journal of Materials Science: Materials in Medicine* **2004**, *15* (9), 1021–1029.

(31) McCarthy, J. R.; Jaffer, F. A.; Weissleder, R. A Macrophage-Targeted Theranostic Nanoparticle for Biomedical Applications. *Small* **2006**, *2* (8–9), 983–987.

(32) Lim, S. Y.; Law, C. S.; Markovic, M.; Kirby, J. K.; Abell, A. D.; Santos, A. Engineering the Slow Photon Effect in Photoactive Nanoporous Anodic Alumina Gradient-Index Filters for Photocatalysis. *ACS Applied Materials and Interfaces* **2018**, *10* (28), 24124–24136.

(33) Law, C. S.; Lim, S. Y.; Abell, A. D.; Voelcker, N. H.; Santos, A. Nanoporous Anodic Alumina Photonic Crystals for Optical Chemo- and Biosensing: Fundamentals, Advances, and Perspectives. *Nanomaterials* **2018**, *8* (10), 1–47.

(34) Krismastuti, F. S. H.; Bayat, H.; Voelcker, N. H.; Schönherr, H. Real Time Monitoring of Layer-by-Layer Polyelectrolyte Deposition and Bacterial Enzyme Detection in Nanoporous Anodized Aluminum Oxide. *Analytical Chemistry* **2015**, *87* (7), 3856–3863.

(35) Kumeria, T.; Santos, A.; Losic, D. Ultrasensitive Nanoporous Interferometric Sensors for Label-Free Detection of Gold (III) Ions. *ACS Applied Materials & Interfaces* **2013**, *5*, 11783–11790.

(36) Popat, K. C.; Mor, G.; Grimes, C. A.; Desai, T. A. Surface Modification of Nanoporous Alumina Surfaces with Poly (Ethylene Glycol). *Langmuir* **2004**, *20* (19), 8035–8041.

(37) Santos, A.; Formentín, P.; Pallarès, J.; Ferré-Borrull, J.; Marsal, L. F. Structural Engineering of Nanoporous Anodic Alumina Funnels with High Aspect Ratio. *Journal of Electroanalytical Chemistry* **2011**, *655* (1), 73–78.

(38) Vojkuvka, L.; Santos, A.; Pallarès, J.; Ferré-Borrull, J.; Marsal, L. F.; Celis, J. P. On the Mechanical Properties of Nanoporous Anodized Alumina by Nanoindentation and Sliding Tests. *Surface and Coatings Technology* **2012**, *206* (8–9), 2115–2124.

(39) Marsal, L. F.; Vojkuvka, L.; Formentin, P.; Pallarés, J.; Ferré-Borrull, J. Fabrication and Optical Characterization of Nanoporous Alumina Films Annealed at Different Temperatures. *Optical Materials* **2009**, *31* (6), 860–864.

(40) Santos, A.; Vojkuvka, L.; Alba, M.; Balderrama, V. S.; Ferré-Borrull, J.; Pallarès, J.; Marsal, L. F. Understanding and Morphology Control of Pore Modulations in Nanoporous Anodic Alumina by Discontinuous Anodization. *Physica Status Solidi (A) Applications and Materials Science* **2012**, *209* (10), 2045–2048.

(41) Macias, G.; Hernandez-Eguia, L. P.; Ferre-Borrull, J.; Pallares, J.; Marsal, L. F. Gold-Coated Ordered Nanoporous Anodic Alumina

Bilayers for Future Label-Free Interferometric Biosensors. *ACS Applied Materials and Interfaces* **2013**, *5* (16), 8093–8098.

(42) Santos, A.; Ferré-Borrull, J.; Pallarès, J.; Marsal, L. F. Hierarchical Nanoporous Anodic Alumina Templates by Asymmetric Two-Step Anodization. *Physica Status Solidi (A) Applications and Materials Science* **2011**, *208* (3), 668–674.

(43) Eckstein, C.; Acosta, L. K.; Pol, L.; Xifré-Pérez, E.; Pallares, J.; Ferré-Borrull, J.; Marsal, L. F. Nanoporous Anodic Alumina Surface Modification by Electrostatic, Covalent, and Immune Complexation Binding Investigated by Capillary Filling. *ACS Applied Materials and Interfaces* **2018**, *10* (12), 10571–10579.

(44) Ruminski, A. M.; Moore, M. M.; Sailor, M. J. Humidity-Compensating Sensor for Volatile Organic Compounds Using Stacked Porous Silicon Photonic Crystals. *Advanced Functional Materials* **2008**, *18* (21), 3418–3426.

(45) Meade, S. O.; Yoon, M. S.; Ahn, K. H.; Sailor, M. J. Porous Silicon Photonic Crystals as Encoded Microcarriers. *Advanced Materials* **2004**, *16* (20), 1811–1814.

(46) Santos, A. Nanoporous Anodic Alumina Photonic Crystals: Fundamentals, Developments and Perspectives. *J. Mater. Chem. C* **2017**, *5* (23), 5581–5599.

(47) Macias, G.; Ferré-Borrull, J.; Pallarès, J.; Marsal, L. F. 1-D Nanoporous Anodic Alumina Rugate Filters by Means of Small Current Variations for Real-Time Sensing Applications. *Nanoscale research letters* **2014**, *9* (1), 315.

(48) Kumeria, T.; Santos, A.; Losic, D. Nanoporous Anodic Alumina Platforms: Engineered Surface Chemistry and Structure for Optical Sensing Applications. *Sensors* **2014**, *14* (7), 11878–11918.

(49) Sahel, S.; Amri, R.; Gamra, D.; Lejeune, M.; Benlahsen, M.; Zellama, K.; Bouchriha, H. Effect of Sequence Built on Photonic Band Gap Properties of One-Dimensional Quasi-Periodic Photonic Crystals: Application to Thue-Morse and Double-Period Structures. *Superlattices and Microstructures* **2017**, 1–9.

(50) Shen, H.; Wang, Z.; Wu, Y.; Yang, B. One-Dimensional Photonic Crystals: Fabrication, Responsiveness and Emerging Applications in 3D Construction. *RSC Adv.* **2016**, *6* (6), 4505–4520.

(51) Kelly, T. L.; Garcia Sega, A.; Sailor, M. J. Identification and Quantification of Organic Vapors by Time-Resolved Diffusion in Stacked Mesoporous Photonic Crystals. *Nano Letters* **2011**, *11* (8), 3169–3173.

(52) Santos, A.; Yoo, J. H.; Rohatgi, C. V.; Kumeria, T.; Wang, Y.; Losic, D. Realisation and Advanced Engineering of True Optical Rugate Filters Based on Nanoporous Anodic Alumina by Sinusoidal Pulse Anodisation. *Nanoscale* **2016**, *8* (3), 1360–1373.

(53) Calvo, M. E.; Colodrero, S.; Hidalgo, N.; Lozano, G.; López-López, C.; Sánchez-Sobrado, O.; Míguez, H. Porous One Dimensional Photonic Crystals: Novel Multifunctional Materials for Environmental and Energy Applications. *Energy and Environmental Science* **2011**, *4* (12), 4800–4812.

(54) Bartzsch, H.; Lange, S.; Frach, P.; Goedicke, K. Graded Refractive Index Layer Systems for Antireflective Coatings and Rugate Filters Deposited by Reactive Pulse Magnetron Sputtering. *Surface and Coatings Technology* **2004**, *180–181*, 616–620.

(55) Alekseev, S. A.; Lysenko, V.; Zaitsev, V. N.; Barbier, D. Application of Infrared Interferometry for Quantitative Analysis of Chemical Groups Grafted onto the Internal Surface of Porous Silicon Nanostructures. *Journal of Physical Chemistry C* **2007**, *111* (42), 15217–15222.

(56) Cheng, W.; Steinhart, M.; Gösele, U.; Wehrspohn, R. B. Tree-like Alumina Nanopores Generated in a Non-Steady-State Anodization. *Journal of Materials Chemistry* **2007**, *17* (33), 3493–3495.

(57) Lee, W.; Kim, J. C. Highly Ordered Porous Alumina with Tailor-Made Pore Structures Fabricated by Pulse Anodization. *Nanotechnology* **2010**, *21* (48), 1–8.